Supporting Information for

Comparative study of the elemental composition of metal-bearing nanomaterials in wildland-urban interface fire ashes using icp-TOF-MS

Mahbub Alam[1*], Sheryl A. Singerling[2], Mahdi Erfani[3], Charles N. Alpers[4], Mohammed Baalousha[1*]

[1] Center for Environmental Nanoscience and Risk, Department of Environmental Health Sciences, Arnold School of Public Health, University of South Carolina, Columbia, South Carolina, U.S.A.

[2] National Center for Earth and Environmental Nanotechnology Infrastructure (NanoEarth), Institute for Critical Technology and Applied Science, Virginia Polytechnic Institute and State University, Blacksburg, Virginia, U.S.A.

[3] Department of Civil and Environmental Engineering, University of South Carolina, SC 29208, U.S.A.

[4] U.S. Geological Survey, California Water Science Center, 6000 J Street, Sacramento, CA 95819, U.S.A.

* Corresponding author: mbaalous@mailbox.sc.edu

Note: Any use of trade, firm, or product names is for descriptive purposes only and does not imply endorsement by the U.S. Government.

1. Meta(loids) in Vegetation and Structural Materials

Metal(loid)s accumulate preferentially in vegetation and are widely used in structural materials. Depending on plant species, a typical plant contains on dry weight basis 100 (range: 50 to 1000) mg kg^{-1} Fe, 50 (20 to 200) mg kg^{-1} Mn, 20 (10-100) mg kg^{-1} Zn, and 6 (2-100) mg kg^{-1} Cu [1]. Another study reported that plants contain 196 (97 to 422) mg kg^{-1} Si, 106 (25 to 355) mg kg^{-1} Al, 75 (37 to 443) mg kg^{-1} Fe, 32 (13 to 205) mg kg^{-1} Zn, 29 (3 to 81) mg kg^{-1} Ba, 5 (2 to 8) mg kg^{-1} Cu, <0.2 mg kg^{-1} Cr, <0.2 mg kg^{-1} As, and 0.042 (0.1 to 4) mg kg^{-1} Pb [2]. Nonetheless, metal(loid) concentrations vary significantly among different plant species due to differences in the accumulative capacity of different vegetation species, taking up distinct levels of elements from the soil and surrounding environment [3, 4]. Metal(loid)s stored in plant tissue could potentially form metal-bearing incidental nanomaterials (INMs) during the combustion of plant material.

Furthermore, metal(loid)s in various forms —bulk, pigments (100-300 nm), and nanomaterials (1-100 nm)— are widely used in the urban environment including human-made structures, vehicles, paints, and coatings. For instance, TiO_2, is widely used as a white pigment in paints and coatings [5]. The global consumption of TiO_2, mainly as pigments, is estimated to be 6.1 million metric tons in 2016 and is projected to reach 8.8 million metric tons by 2025 [5], with major uses in architectural and industrial paints and coatings (60%), plastic (28%), paper, (5%), and other applications (7%) [5, 6]. Iron oxides are also widely used as pigment in paints, coatings, and construction material such as concrete products, mortar, paving stones, and roofing tiles. Iron oxide pigments are used as colorants for ceramic glazes, glass, paper, plastic, rubber, and textiles and in cosmetics and magnetic ink toner [7]. The total consumption of iron oxide pigments in the United States was approximately 200,000 tons in 2020 [8]. Chromated copper arsenate (CCA, CrO_3, CuO, and As_2O_5) was widely used as a wood preservative or in pesticides since the 1940s [9-14]; the use of CCA-treated wood in residential construction in the U.S. was greatly reduced starting in late 2003 based on a voluntary agreement by manufacturers [15]. Many other metal(loid)s are also used as pigments and fillers in paints and coatings including Fe oxides, BaO, Al_2O_3, SiO_2, ZnO, $CaCO_3$, and aluminum silicates.

In addition to the use of pure metal-bearing particles as pigments, metal alloys (mixtures of metals with metals or other elements at specific ratios) are also widely used in a variety of applications because they offer better durability, strength, and corrosion resistance compared to the pure metals [16, 17]. An alloy is distinct from an impure metal in that the added elements are well controlled to produce desirable properties. In contrast, the composition of impure metals is less controlled. Stainless steel is an iron (74-90%) alloy with Cr (10-20%), Mo, V, or Ni (5-15%), which is widely used in household appliances such as refrigerators and gas stoves, cookware cutlery, surgical instruments. Bronze is a copper (85-88%)-tin (12-25%) alloy, and brass is a copper (66.6%)-zinc (33.3%) alloy; bronze and brass are widely used in construction material, home decoration, and automobiles. Aluminum alloys are made by combining aluminum (99%) with small amounts (1%) of elements such as Mn, Cu, Mg, Si, Zn and Co. Several hundred different aluminum alloys exist and are used in a wide range of applications including automobiles, airplanes, medical equipment, consumer products, wiring, and electronics. Copper (70-90%)-nickel (10-30%) alloys are effective electrical conductors, corrosion resistant, and have a high tensile strength. They are commonly used in electronics, batteries, relays, solder frames, marine applications, and oil and gas pipelines. Tin (90-99%)-Sb (1-10%) alloys are used in bearing assembly, casting, and step soldering, a common method for making printed circuit board assemblies. Lead (90-99%)-Sb (1-10%) alloys used in bearings, step soldering, and storage-battery plates [18]. Lead (67%)-Sn (33%) alloys are/were widely used in solder [18]. The alloy compositions summarized above can vary significantly and many other compositions are available on the market and are documented in the literature [16, 17].

Fire at the WUI transforms fuels (*i.e.*, vegetation, soil organic matter, and construction material) into materials with different chemical and physical properties, including ash, black carbon, methane, carbon monoxide, and carbon dioxide [19]. Ash is the particulate residue after fire that remains in situ, is transported in air, or is deposited on the ground, and consists of minerals and charred organic materials [19]. The quantity, elemental composition, and properties of ash produced during a fire depend on burned fuel and combustion completeness [20]. Ash formed at low combustion temperatures (*e.g.*, < 450 ºC) are rich in organic carbon and are thus black, whereas ashes formed at high combustion temperatures (*e.g.*, > 450 ºC) are rich in

inorganic minerals such as calcium, magnesium, sodium, potassium, silicon, and phosphorus, mostly carbonates [21-23]. Ashes formed at higher combustion temperatures (*e.g.*, > 850 ºC) contain mainly inorganic oxides [19].

2. Materials and Methods

2.1. Study Sites

Table S1. Description of ashes collected following the 2020 fire season.

Sample label for this study	Sample number used in previous studies	Sampling date	Ash Source	Sample description
A1	A31	10/8/2020	Vegetation	Burned chaparral (charred manzanita and some pine) site on gentle slopes; serpentinite unit
A2	A81	10/8/2020	Vegetation	Burned oak, white ash with some black ash; bedrock undetermined
A3	AD		Atmospheric deposition	Ash deposited on a car windshield
A4	A92	10/15/2020	Structure	Red soil - artificial wood from deck
A5	A122	10/15/2020	Structure	Studio - some burned paint (acrylic and watercolor) blues, yellow, red
A6	A124	10/15/2020	Structure	Shed - house paint, some wires
A7	A13	10/7/2020	Vehicle	Burned trailer - south end
A8	A131	10/16/2020	Structure/vehicle	Burned barn - redwood, galvanized steel, tires, Cu wire
A9	A132	10/16/2020	Structure/vehicle	Burned tool storage shed - tires, white & black ash, misc. bags & containers

Ash name used in previous studies [20, 24] is provided for ease of comparison. All samples collected in LNU Lightning Complex fire area except A3 (North Complex Fire [20, 24], located between Quincy and Oroville, California, approximately 100 km northeast of LNU Lightning Complex Fire).

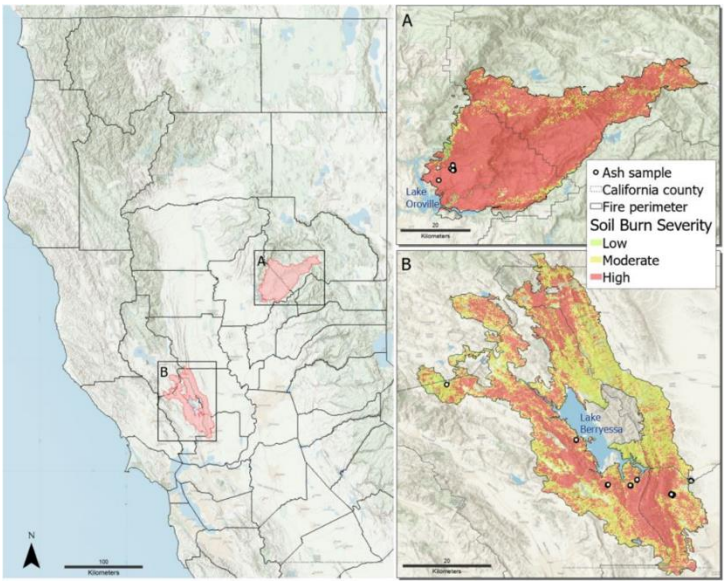

Figure S1. Maps of soil burn severity in the two fires investigated in this study (A) the North Complex (NC) Fire and (B) the LNU Lightning Complex Fire. The left panel displays the location of the burned areas in northern California. Base maps from https://www.mtbs.gov/.

2.2. Bulk metal concentration

One hundred mg of each sample was weighed into a polytetrafluoroethylene (PTFE) digestion vessel. Digestion reagents were added in the following order: 9 ml of distilled HNO_3, 3 ml of distilled HF, and 2 ml of H_2O_2. The acid digestion was performed in a Multiwave microwave (Multiwave Pro, Anton Paar, Graz, Austria) at a constant power of 1500 W for 60 minutes, preceded by a 15-minute ramping time to reach the desired power. The digestate was then evaporated in two steps using the same microwave system to remove non-reacted HF. The first evaporation was performed with 10 minutes of ramping time followed by 9 minutes of holding time at 1500 W. Then, 3 ml of distilled HNO_3 were added into the vessel to dissolve any insoluble fluoride salts. The second evaporation was performed with 10 minutes of ramping time followed by 3 minutes of holding time at 1500 W. The digested samples were then diluted in 10% HNO_3 (trace metal grade, Fisher Chemical, Fair Lawn, New Jersey, USA) and stored until total metal analysis.

Total metal concentrations were determined using an inductively coupled plasma-time of flight-mass spectrometer (ICP-TOF-MS, TOFWERK, Switzerland). Mass spectra calibration and routine tuning were performed prior to analysis every day to achieve maximum sensitivity. Elemental concentration calibration was established using a series of ionic standards prepared in 1% HNO_3 from commercially available ICP multi-element standards (BDH Chemicals, Radnor, Pennsylvania, USA). Internal standards (ICP Internal Element Group Calibration Standard, BDH Chemicals, Radnor, Pennsylvania, USA) were applied to monitor signal drift for quality control. The instrument operating conditions are presented in **Table S2,** and the monitored isotopes are listed in **Table S3**. Dissolved multi-element standards were prepared in 1% HNO_3 from commercially available ICP standards (BDH Chemicals, Radnor, Pennsylvania, USA), with concentrations ranging from 0.001 to 100 μg L^{-1}. Internal standards (ICP Internal Element Group Calibration Standard, BDH Chemicals, Radnor, Pennsylvania, USA) were monitored simultaneously for quality control. All isotopes were analyzed in collision mode with a helium and hydrogen gas mixture.

2.3. Cloud point extraction of incidental nanomaterials

Nanomaterials were extracted from ashes using cloud point extraction following the protocol described elsewhere [25]. Briefly, 100 mg of each ash sample were suspended in 10 mL 0.2% (by weight) FL-70 surfactant in 15 mL acid-washed centrifuge tubes, followed by overhead rotation for 2 hours at 40 rpm (Mark and Model), 60 minutes batch sonication with ice water (Branson 2800, 40 kHz, Danbury, Connecticut, USA) to disperse NNMs, and centrifugation at 1,000 g for 2 minutes (Eppendorf, 5810R, Hamburg, Germany) to obtain < 1 μm particle fraction (assuming natural particle density of 2.5 g cm^{-3}). The top 7 mL supernatant was transferred into acid-washed 15 mL centrifuge tubes. Then an additional surfactant, Triton X-114, and NaCl were added to the extract to achieve a final concentration of 0.2% and 1 mM, respectively. The mixture was then heated at 50 °C for 1 hour to form micelles. The suspension was centrifuged at 1000 g for 5 minutes to create 2 phases: a surfactant-enriched phase containing the NMs and water phase containing the ions. The surfactant-enriched phase containing NMs was separated and refrigerated at or below 4 °C before single particle (SP)-ICP-TOF-MS analysis. The theoretical size of the extracted fractions corresponds to particles < 1000 nm for natural particles (assuming a density of 2.5 g cm^{-3}). All samples were bath sonicated again for 15 min and were diluted by a factor of 100,000 prior to SP-ICP-TOF-MS analysis to avoid coincidence and eliminate dissolved background.

Table S2. Operating conditions for inductively coupled plasma-time of flight-mass spectrometer (ICP-TOF-MS) analysis for conventional (dissolved metal concentration) and single particle analysis modes.

Instrument parameter	**Total concentration analysis**					**Single particle analysis**				
Plasma Power	1550 W					1550 W				
Nebulizer Gas Flow	1.10-1.14 L/min					1.10-1.14 L/min				
Auxiliary Gas Flow	0.8 L/min					0.8 L/min				
Cooling Gas Flow	14 L/min					14 L/min				
Injector Diameter	2.5 mm					2.5 mm				
Collision Cell Gas	5 mL/min He with 4.5% H_2					5 mL/min He with 4.5% H_2				
CCT Bias	-2.00 to -4.00 V					-2.00 to -4.00 V				
Notch	Mass	29	32	36.3	41	Mass	29	32	36.3	41
	Amplitude (V)	1.6	2.0	2.0	1.2	Amplitude (V)	1.6	2.0	2.0	1.2
TOF Repetition Rate	33 kHz					33 kHz				
Detected Mass Range	14-275 m/Z					14-275 m/Z				
(CeO/Ce)	< 4.0%					< 3.0%				
Data Acquisition	Continuous Mode					Continuous Mode				
TOF Time Resolution	0.3 s					30 µs				
Integration Time	0.3 s					2 ms				
Acquisition Time	60 s					200-300 s				
Sample Flow Rate	-					0.455 mL/min				
Transport Efficiency	-					6.6% (5-7%)				

Table S3. Elements monitored for single particle-inductively coupled plasma-time of flight-mass spectrometer (SP-ICP-TOF-MS) analysis and the corresponding particle mass and size detection limits.

Element	Isotope	Mass detection limit (g)	Size detection limit (nm, assuming pure metallic particle)	Size detection limit (nm, assuming pure metal oxide particle)	Metal oxide form
Al	^{27}Al	1.72-1.94 × 10^{-14}	230-239	250-261	Al_2O_3
Si	^{28}Si	7.82-8.90 × 10^{-14}	400-418	494-516	SiO_2
Ti	^{48}Ti	6.69-7.15 × 10^{-16}	66-67	80-81	TiO_2
V	^{51}V	4.49-4.74 × 10^{-16}	52-53	77-78	V_2O_5
Cr	^{52}Cr	4.21-4.54 × 10^{-16}	48-49	61-62	Cr_2O_3
Mn	^{55}Mn	2.83-2.92 × 10^{-16}	42-43	55-56	MnO_2
Fe	^{56}Fe	4.30-4.96 × 10^{-16}	47-48	61-64	Fe_2O_3
Co	^{59}Co	2.59-2.64 × 10^{-16}	38	48	Co_3O_4
Ni	^{60}Ni	1.05-1.06 × 10^{-15}	61	73	NiO
Cu	^{65}Cu	8.27-8.49 × 10^{-16}	56-57	68-69	CuO
Zn	^{66}Zn	1.12-1.21 × 10^{-15}	67-69	78-80	ZnO
As	^{75}As	1.65-1.70 × 10^{-15}	82-83	104-105	As_2O_5
Zr	^{90}Zr	3.74-3.98 × 10^{-16}	48-49	55-57	ZrO_2
Nb	^{93}Nb	1.40-1.44 × 10^{-16}	31-32	43	Nb_2O_5
Sn	^{120}Sn	3.12-3.22 × 10^{-16}	43-44	48	SnO_2
Sb	^{121}Sb	2.68-2.71 × 10^{-16}	42-43	49	Sb_2O_3
Ba	^{138}Ba	1.07-1.68 × 10^{-16}	37-45	33-40	BaO
La	^{139}La	7.05-7.19 × 10^{-17}	28	29	La_2O_3
Ce	^{140}Ce	8.51-8.90 × 10^{-17}	29	31-30	CeO_2
Pr	^{141}Pr	6.00-6.10 × 10^{-17}	26	28	Pr_6O_{11}
Nd	^{142}Nd	1.70-1.76 × 10^{-16}	36	37-38	Nd_2O_3
Gd	^{158}Gd	2.89-2.90 × 10^{-16}	41	44	Gd_2O_3
Dy	^{164}Dy	2.01-2.02 × 10^{-16}	36	38	Dy_2O_3
Ho	^{165}Ho	5.79-5.80 × 10^{-17}	23	25	Ho_2O_3
Er	^{166}Er	1.84-1.85 × 10^{-16}	34	36	Er_2O_3
Hf	^{180}Hf	2.03-2.05 × 10^{-16}	31	36	HfO_2
Ta	^{181}Ta	1.54-1.55 × 10^{-16}	26	35	Ta_2O_5
W	^{184}W	4.14-4.15 × 10^{-16}	35	44	WO_2
Pb	^{208}Pb	1.52-1.84 × 10^{-16}	29-31	32-34	PbO
Th	^{232}Th	8.28-8.29 × 10^{-17}	24	26	ThO_2
U	^{238}U	8.01-8.09 × 10^{-17}	20	25	UO_2

Particle mass detection limit is calculated according to the Poisson distribution = $Mass_{detection\ limit} = 3.29\sqrt{background\ signal} + 2.71$. The mass detection limit is calculated based on the element background signal in the samples. The DL for each element varied within a narrow range between the different samples due to the significant dilution (100,000 folds) of the samples.

Size detection limit is calculated as the equivalent spherical diameter from the particle mass detection limit assuming pure metal and metal oxide phases.

3. Results and Discussion

3.1. Single Particle Elemental Composition

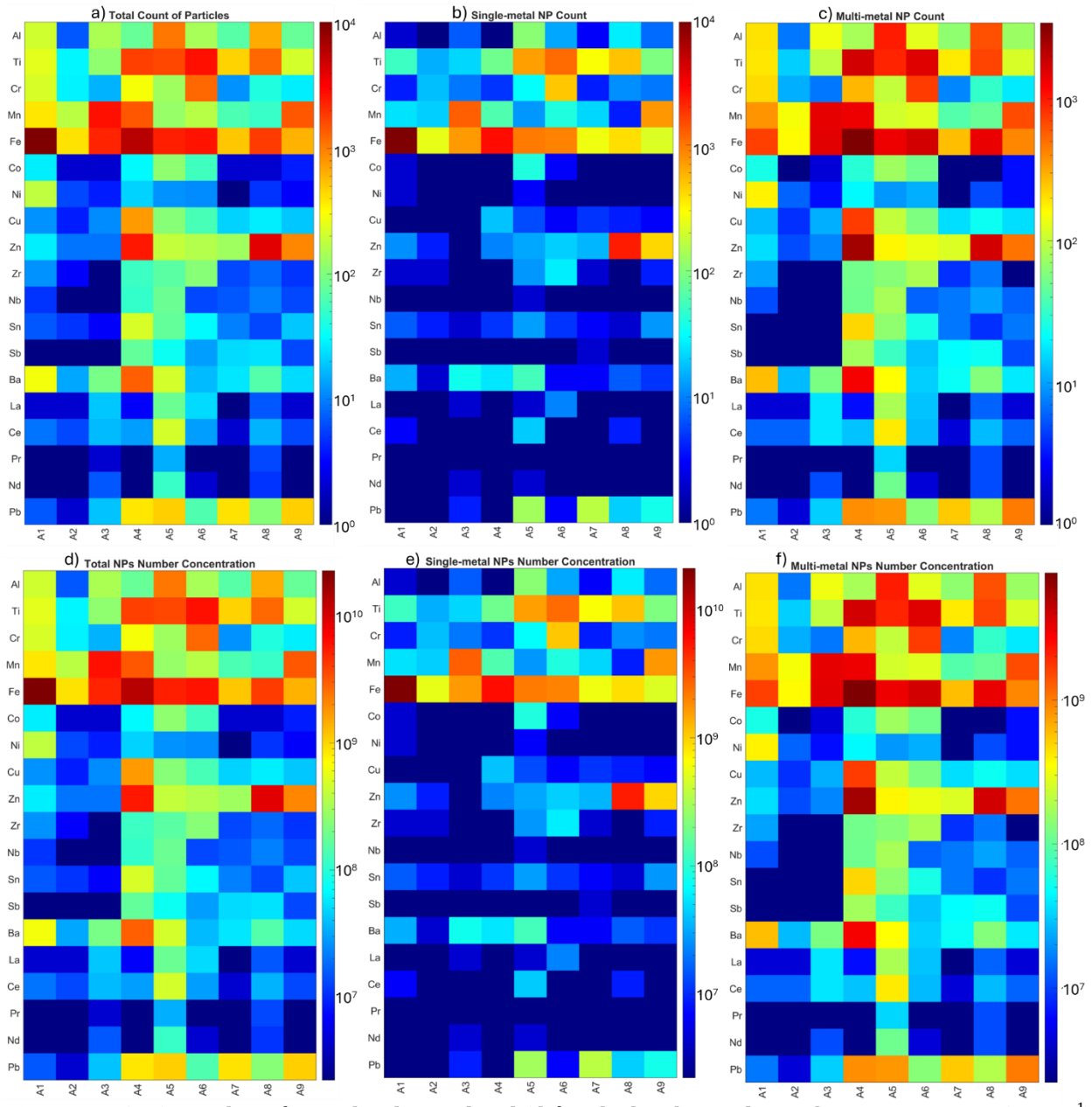

Figure S2. (a-c) Number of particles detected and (d-f) calculated particle number concentration (NM g^{-1}) in wildland-urban interface fire ashes using single particle-time of flight-mass spectrometer: (a and d) total, (b and e) single metal nanomaterials (smNM), (c and f) multi-metal nanomaterials (mmNMs) in fire ashes at the wildland-urban interface (WUI). A1 and A2 are vegetations ashes, A3 is an atmospheric deposition ash, A4, A5, and A6 are structural ashes, and A7 is a vehicle ash, and A8 and A9 are mixed structural and vehicle ashes.

3.2. Multi Metal Nanomaterial Clusters

The most dominant mmNM clusters were FeMnZn, FeMn, TiFeZn, AlFeZn, MnFeZn, and CrFeMn. These clusters are described in more detail in this section.

Fe-rich mmNM clusters. The FeMnZn cluster accounts for 77-95% of mmNMs in vegetation and structural ashes (A1, A2, and A4) and < 21% of mmNMs in all other ashes (**Figure 1b**). The FeMn cluster accounts for 91% of all mmNM in the atmospheric deposition ash. Fe accounts for 65 to 80% of the total elemental mass of mmNMs in the FeMnZn cluster, whereas Mn accounts for 1-19%. In contrast, Fe and Mn account for nearly 50% each of the total elemental mass of mmNMs in the FeMn cluster. Additionally, elements such as Zn, Ti, Pb, Cr, and Cu are detected in the FeMnZn cluster. These observations demonstrate a contribution of anthropogenic NMs to the FeMnZn clusters.

Ti-rich mmNM cluster. The TiFeZn cluster accounts for 2 to 8% of mmNMs in vegetation, 0% mmNMs in the atmospheric deposition ashes, 19 to 62% of mmNMs in structural ashes, and 4 to 39% of mmNMs in vehicle ashes. Ti accounts for 63 to 94% of mmNM masses, whereas Fe accounts for 1 to 36% of mmNM masses. The elemental ratios of Ti/Fe are generally higher than the natural ratios [26] in all samples; Ti/Fe ratios highest in vehicle ashes (median: 7.2 to 17.2, range: 0.5 to 370) and lowest in vegetation ashes (median: 1.5, range: 0.4 to 117); Ti/Fe ratios in structural ashes ranged from 0.4 to 1024 with a median Ti/Fe from 2.6 to 7.7. These values are higher than the average crustal Ti/Fe ratio [27] and Ti/Fe ration in natural mmNMs [26]. Additionally, mmNMs within the TiFeZn cluster contain Zn, Pb, and Cr, indicating an anthropogenic INM contribution.

Al-rich mmNM cluster. The AlFeZn cluster accounts for 1 to 57% of mmNMs in structural ashes, 6 to 35% of mmNMs in vehicle ashes, and 0 to 9% in vegetation and atmospheric deposition ashes. The elemental ratios of Al/Fe are higher in the structural and vegetation ashes (1 to 200 with a median of 12 to 23) than in the vegetation and atmospheric deposition ashes (0.05 to 15 with a median of 2.0 to 4.0). The latter is close to the average cluster Al/Fe ratio [27]. Additionally, the AlZnFe cluster contains Zn, Ti, Pb, Cr, and Cu which indicates an anthropogenic INM contribution.

Mn-rich mmNM cluster. The MnFeZn cluster accounts for 46% of all mmNMs in one of the vehicle ashes (A9) and <2% of all mmNMs in all other ashes. Multi-metal NMs within the MnFeZn cluster are associated with Zn, Pb, Cu, Ni, Co, Sn, and Cr, which indicates an anthropogenic origin of this cluster, most likely from vehicle components such as brake pads [28].

Cr-rich mmNM cluster. The CrFeMn cluster accounts for 12% of all mmNMs in one of the structural ashes (A6) and < 1% in all other samples. Multi-metal NMs within the CrFeMn cluster are associated with Fe, Mn, Cu, Zn, Pb, Ti, Sb, Al, and Ba, with Cr, Mn, Fe, Cu, and Zn accounting for 65 to 84%, <24%, <21%, < 16%, and <11% of the mass of mmNMs within the CrFeMn cluster, respectively. The CrFeMn cluster is most likely comprised of heteroaggregates of multiple smNMs and mmNMs. All other mmNM clusters account for a small fraction of all mmNMs within the ash samples.

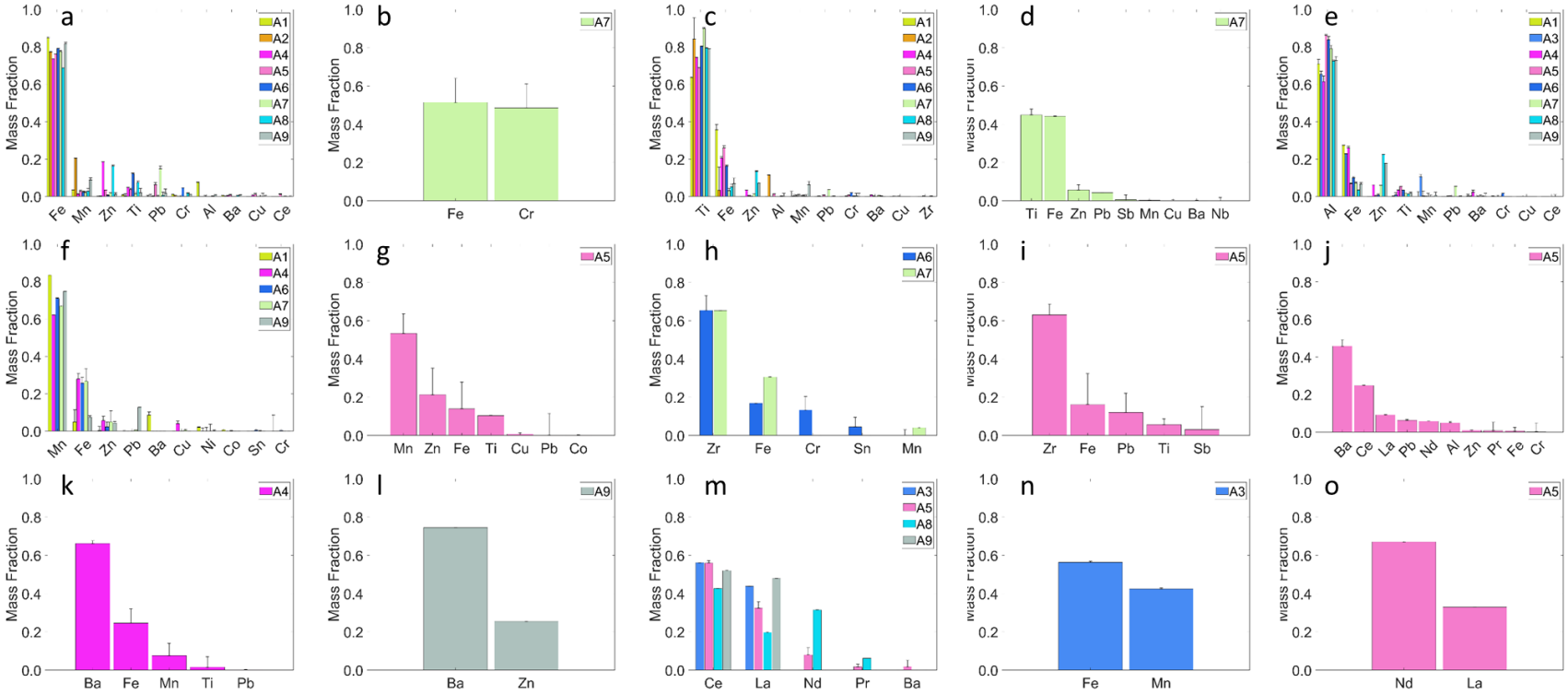

Figure S3. Mean mass fraction of elements within multi-metal nanomaterials (mmNMs) clusters: (a, b, and n) Fe-rich, (c and d) Ti-rich, (e) Al-rich, (f and g) Mn-rich, (h and i) Zr-rich, (j-l) Ba-rich, (m) Ce-rich, (o) Nd-rich mmNM clusters. First and second stage clustering cutoffs were 0.3 to 0.6 and 0.089, respectively. The distance cutoff refers to the specific point on the clustering dendrogram where the hierarchy is cut to determine the final clusters, defining the maximum distance at which two subclusters will be considered part of a major cluster. Further details can be found in previous publications [28].

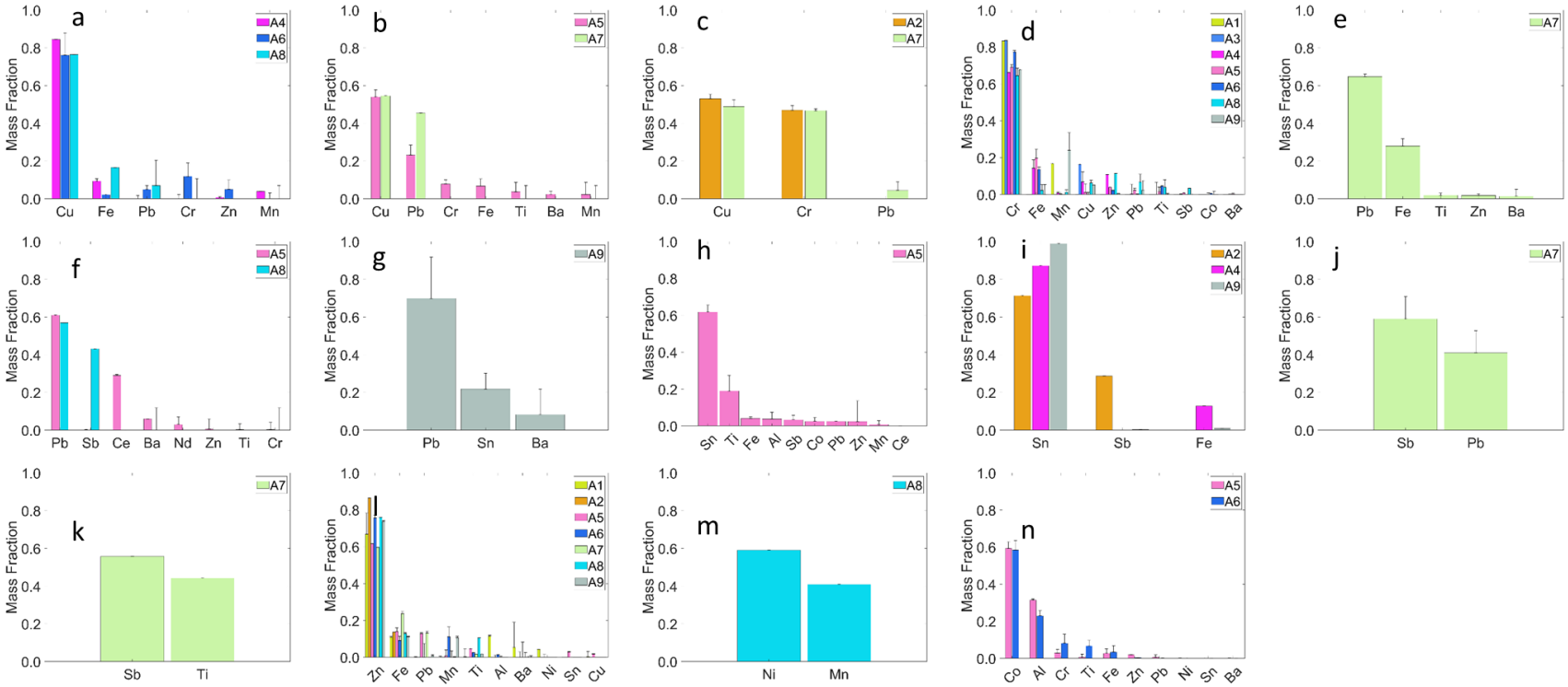

Figure S4. Mean mass fraction of elements within multi-metal nanomaterial (mmNM) clusters: (a-c) Cu-, (d) Cr-, (e-g) Pb-, (h and i) Sn-, (j and k) Sb-, (l) Zn-, (m) Ni, and (n) Co-rich mmNM clusters. First and second stage cutoffs were 0.3 to 0.6 and 0.089, respectively.

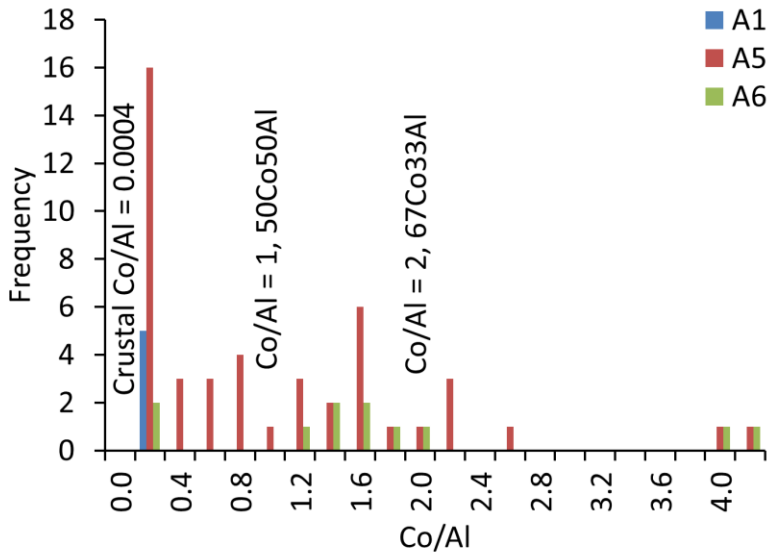

Figure S5. Elemental ratio of Co/Al.

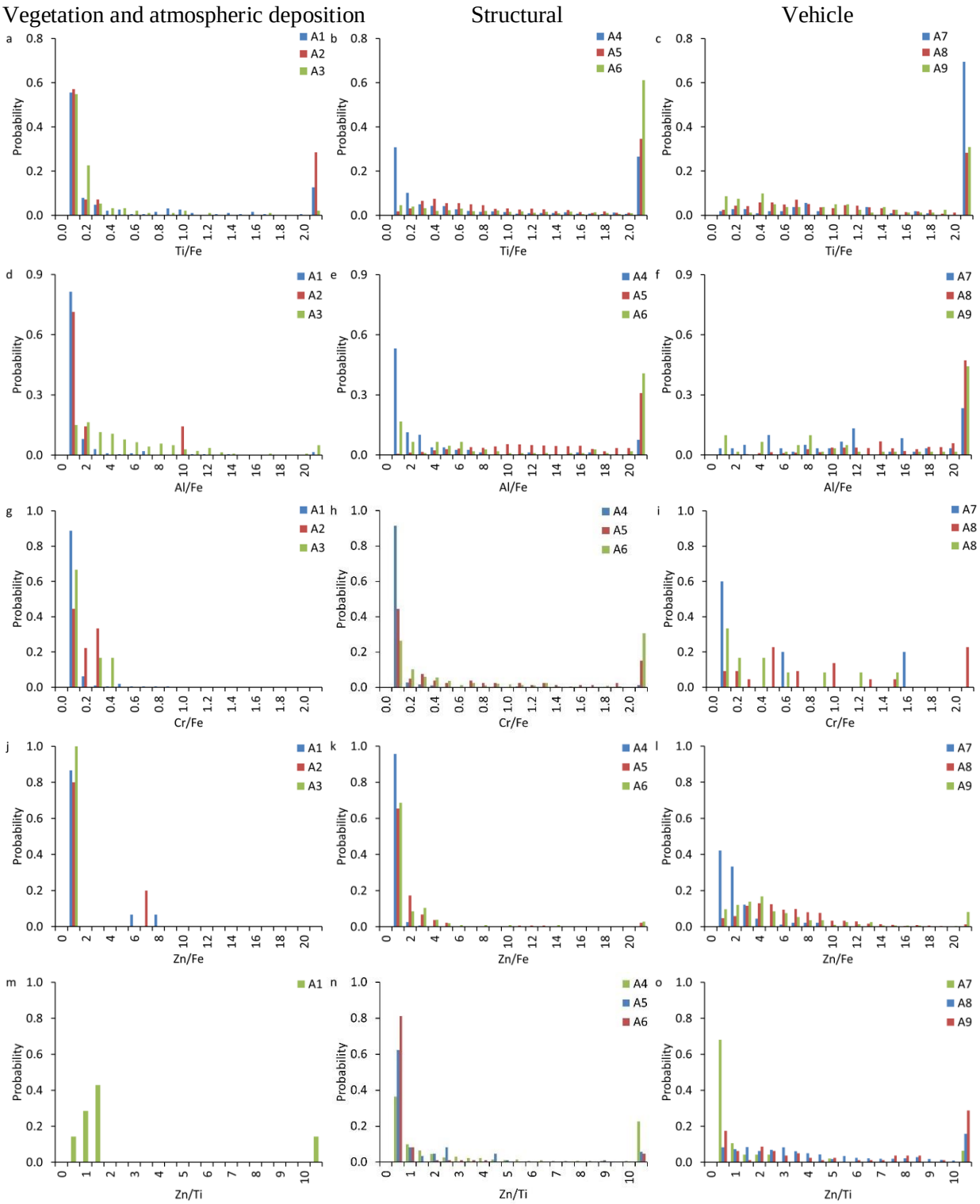

Figure S6. Elemental ratios of (a-c) Ti/Fe (n = 14 to 1705), (d-f) Fe/Al (n = 7 to 885), (g-i) Cr/Fe (n = 5 to 620), (j-l) Zn/Fe (n = 5 to 2562), and (m-o) Zn/Ti (n = 7 to 1159) in (a, d, g, j, m) vegetation and atmospheric deposition ash, (b, e, h, k, n) structural ash, and (c, f, i, l, o) vehicle ash. n: number of detected particles by single particle-inductively coupled plasma-time of flight-mass spectrometer (SP-ICP-TOF-MS).

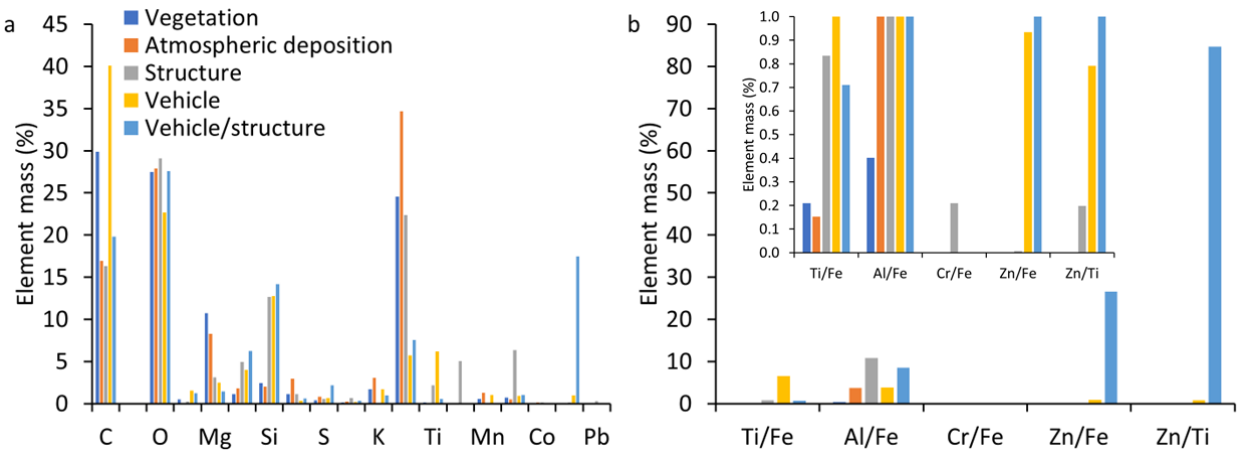

Figure S7. Average overall aggregate elemental compositions and ratios obtained on INM aggregates by transmission electron microscopy (TEM) coupled with energy dispersive spectroscopy (EDS).

Table S4. Overall aggregate elemental compositions and ratios obtained on INM aggregates by transmission electron microscopy (TEM) coupled with energy dispersive spectroscopy (EDS).

Sample	Aggregate	C	N	O	Na	Mg	Al	Si	P	S	Cl	K	Ca	Ti	Cr	Mn	Fe	Co	Zn	Pb	Ti/Fe	Al/Fe	Cr/Fe	Zn/Fe	Zn/Ti
Vegetation		29.9	nd	27.5	0.5	10.8	1.1	2.4	1.1	0.4	0.1	1.7	24.5	0.1	nd	0.5	0.7	nd	nd	nd	0.2	0.4	0.0	0.0	0.0
Atmospheric deposition		16.9	nd	27.9	0.1	8.3	1.8	2.0	3.0	0.8	0.2	3.1	34.7	0.1	nd	1.3	0.5	0.1	nd	nd	0.2	3.7	0.0	0.0	0.0
Structure		16.3	nd	29.1	0.2	3.1	4.9	12.7	1.1	0.5	0.7	0.1	22.4	2.2	5.0	nd	6.3	0.1	0.2	0.3	0.8	10.8	0.2	0.0	0.2
Vehicle		40.1	nd	22.7	1.6	2.5	4.0	12.8	0.3	0.7	0.2	1.7	5.7	6.2	nd	1.1	0.9	nd	1.0	nd	6.6	3.8	0.0	0.9	0.8
Vehicle/structure		19.8	nd	27.6	1.2	1.5	6.2	14.2	0.6	2.2	0.3	0.9	7.5	0.5	nd	nd	1.0	nd	17.5	nd	0.7	8.5	0.0	26.5	84.7
A1	1	21.08	nd	33.42	0.02	26.52	nd	0.79	0.29	0.40	0.09	0.48	16.45	nd	nd	nd	0.47	nd	nd	nd	0.0	0.0	0.0	0.0	0.0
A1	2	29.18	nd	28.53	nd	20.68	nd	0.45	1.11	0.21	nd	0.47	18.98	0.09	nd	nd	0.29	nd	nd	nd	0.3	0.0	0.0	0.0	0.0
A1	3	35.87	nd	26.47	nd	17.38	0.51	1.10	0.48	0.40	nd	0.83	15.45	nd	nd	nd	1.50	nd	nd	nd	0.0	0.3	0.0	0.0	0.0
A1	5	36.79	nd	25.83	nd	17.19	0.17	1.61	0.61	0.94	nd	1.02	15.15	nd	nd	nd	0.70	nd	nd	nd	0.0	0.2	0.0	0.0	0.0
A1	6	42.27	nd	22.75	nd	7.14	nd	1.12	0.20	nd	nd	0.25	26.26	nd	nd	nd	nd	nd	nd	nd	0.0	0.0	0.0	0.0	0.0
A2	1	43.81	nd	22.23	nd	4.11	nd	0.88	0.14	0.23	nd	0.19	27.84	0.09	nd	0.32	0.15	nd	nd	nd	0.6	0.0	0.0	0.0	0.0
A2	2	24.42	nd	29.33	0.66	2.61	5.18	19.45	0.08	0.30	nd	8.87	6.44	nd	nd	nd	2.67	nd	nd	nd	0.0	1.9	0.0	0.0	0.0
A2	3	47.95	nd	21.49	nd	3.20	0.25	0.60	0.66	0.24	nd	0.29	24.61	0.11	nd	0.23	0.37	nd	nd	nd	0.3	0.7	0.0	0.0	0.0
A2	4	16.69	nd	34.16	0.80	7.83	0.16	0.23	4.37	0.30	nd	1.88	32.32	0.13	nd	0.89	0.23	nd	nd	nd	0.6	0.7	0.0	0.0	0.0
A2	5	14.21	nd	28.24	0.44	7.51	nd	0.36	3.71	0.45	0.17	3.62	40.31	0.08	nd	0.59	0.31	nd	nd	nd	0.3	0.0	0.0	0.0	0.0
A2	6	16.09	nd	29.68	nd	4.08	0.35	0.25	0.96	0.25	nd	0.67	46.19	0.18	nd	0.64	0.66	nd	nd	nd	0.3	0.5	0.0	0.0	0.0
A3	1	25.69	nd	29.31	0.06	3.73	1.58	5.51	1.23	0.30	nd	2.07	29.37	0.10	nd	0.53	0.53	nd	nd	nd	0.2	3.0	0.0	0.0	0.0
A3	4	15.35	nd	27.57	nd	9.80	0.28	0.13	1.22	0.58	nd	0.87	41.88	0.04	nd	1.87	0.40	nd	nd	nd	0.1	0.7	0.0	0.0	0.0
A3	5	9.90	nd	23.55	0.10	18.02	0.87	1.72	5.94	0.65	0.22	10.60	26.83	nd	nd	1.24	0.36	nd	nd	nd	0.0	2.4	0.0	0.0	0.0
A3	6	17.93	nd	28.68	nd	5.67	4.03	nd	2.33	1.33	nd	0.75	38.11	0.16	nd	0.44	0.43	0.13	nd	nd	0.4	9.4	0.0	0.0	0.0
A3	7	15.83	nd	30.33	nd	4.24	2.27	0.63	4.04	1.28	nd	1.09	37.13	0.08	nd	2.30	0.78	nd	nd	nd	0.1	2.9	0.0	0.0	0.0
A5	4	13.90	nd	29.35	0.17	0.73	9.74	18.59	nd	0.72	0.25	0.08	25.24	0.84	nd	nd	0.39	nd	nd	nd	2.2	25.0	0.0	0.0	0.0
A5	5	24.95	nd	29.25	nd	0.83	6.60	14.33	0.13	0.18	0.58	0.09	22.26	0.28	nd	nd	0.37	0.14	nd	nd	0.8	17.8	0.0	0.0	0.0
A5	6	12.13	nd	27.57	0.20	4.17	3.09	6.52	2.09	0.69	1.14	nd	30.76	0.19	5.02	nd	6.00	nd	0.15	0.28	0.0	0.5	0.8	0.0	0.8
A6	1	14.20	nd	30.20	0.36	6.63	0.35	11.22	nd	nd	nd	nd	11.16	7.31	nd	nd	18.56	nd	nd	nd	0.4	0.0	0.0	0.0	0.0
A7	1	22.20	nd	26.37	nd	4.83	2.89	11.35	0.48	0.72	nd	0.71	13.22	14.24	nd	1.05	0.87	nd	1.05	nd	16.4	3.3	0.0	1.2	0.1
A7	2	16.92	nd	33.51	2.69	1.94	7.85	22.83	0.30	0.48	nd	3.55	2.59	4.28	nd	nd	1.35	nd	1.72	nd	3.2	5.8	0.0	1.3	0.4
A7	3	81.10	nd	8.10	0.41	0.69	1.31	4.15	0.22	0.82	0.19	0.80	1.32	0.10	nd	nd	0.59	nd	0.19	nd	0.2	2.2	0.0	0.3	1.9
A8	1	35.75	nd	25.96	nd	4.49	5.91	20.61	0.12	0.40	0.03	0.50	0.99	0.11	nd	nd	1.12	nd	4.01	nd	0.1	5.3	0.0	3.6	36.5
A8	2	8.73	nd	34.31	nd	0.33	12.03	25.10	0.15	0.72	nd	1.09	3.02	0.50	nd	nd	0.82	nd	13.20	nd	0.6	14.7	0.0	16.1	26.4
A8	11	11.11	nd	35.75	nd	0.99	10.57	22.06	0.14	2.07	nd	0.52	4.23	0.84	nd	nd	0.74	nd	11.00	nd	1.1	14.3	0.0	14.9	13.1
A8	12	16.92	nd	34.96	nd	0.77	7.17	14.93	0.15	1.86	nd	0.35	11.79	0.12	nd	nd	0.52	nd	10.45	nd	0.2	13.8	0.0	20.1	87.1
A9	1	22.82	0.57	28.27	1.73	1.11	4.31	9.14	1.30	2.56	0.25	0.81	9.86	nd	nd	nd	3.82	nd	13.45	nd	0.0	1.1	0.0	3.5	∞
A9	2	19.57	nd	21.87	0.69	1.93	4.05	9.36	0.17	1.54	0.47	0.39	10.40	1.44	nd	nd	0.62	nd	27.50	nd	2.3	6.5	0.0	44.4	19.1
A9	3	30.18	nd	20.56	nd	0.59	4.57	10.24	0.26	2.13	0.36	1.62	6.06	0.14	nd	nd	0.55	nd	22.75	nd	0.3	8.3	0.0	41.4	162.5
A9	4	23.07	nd	23.65	nd	2.59	3.80	7.76	2.97	6.61	0.63	1.30	20.13	0.96	nd	nd	0.65	nd	5.88	nd	1.5	5.8	0.0	9.0	6.1
A9	5	10.04	nd	22.64	nd	0.37	3.62	8.17	0.31	1.58	0.21	1.95	1.42	0.15	nd	nd	0.57	nd	48.99	nd	0.3	6.4	0.0	85.9	326.6

Table S5. Transmission electron microscopy (TEM) data for aggregates and metallic INMs in all ash samples except A4.

Ash	Ash source	Aggregates analyzed	Aggregates with INMs	Non-INM components	INM type	INM sizes
A1	Vegetation	6	0	Ca-carbonate	None	N/A
A2	Vegetation	6	0	Ca-carbonate	None	N/A
A3	Atmospheric Deposition	6	1	Al,K-silicates; Ca-carbonates	Rare Mn	N/A
A5	Structure	4	4	Al,Mg,Ca-silicates; Ca-carbonates	Abundant Ti; occasional Cr, Fe, Cu; rare Pb	Ti: 40 to 250 nm (n = 18) Cr: 180 to 270 nm (n = 3) Fe: 190 to 270 nm (n = 2) Cu: 10 to 50 nm (n = 13)
A6	Structure	1	1	Mg-silicates; Ca-carbonates	Abundant Ti, Fe; occasional Cr, Cu	Ti: 190 to 440 nm (n = 13) Fe: 280 to 1070 nm (n = 6) Cr: 90 to 140 nm (n = 2)
A7	Vehicle	3	3	Al-silicates; Ca-carbonates; C (turbostratic)	Abundant Ti, Zn(+Cu+Fe); rare Mn	Ti: 80 to 490 nm (n = 18) Zn(+Cu+Fe): 120 nm (n = 1)
A8	Structure/Vehicle	7	7	Al-silicates; Ca-sulfates; C (turbostratic)	Abundant Ti, Zn	Ti: 50 to 480 nm (n = 17) Zn: 50 to 250 nm (n = 17)
A9	Structure/Vehicle	5	5	Al-silicates; Ca-sulfates; C	Abundant Ti, Fe, Zn(+Cu)	Ti: 140 to 300 nm (n = 7) Fe: < 50 nm (many) Zn(+Cu): 70 to 450 nm (n = 13) and < 50 nm (many)

N/A: not applicable

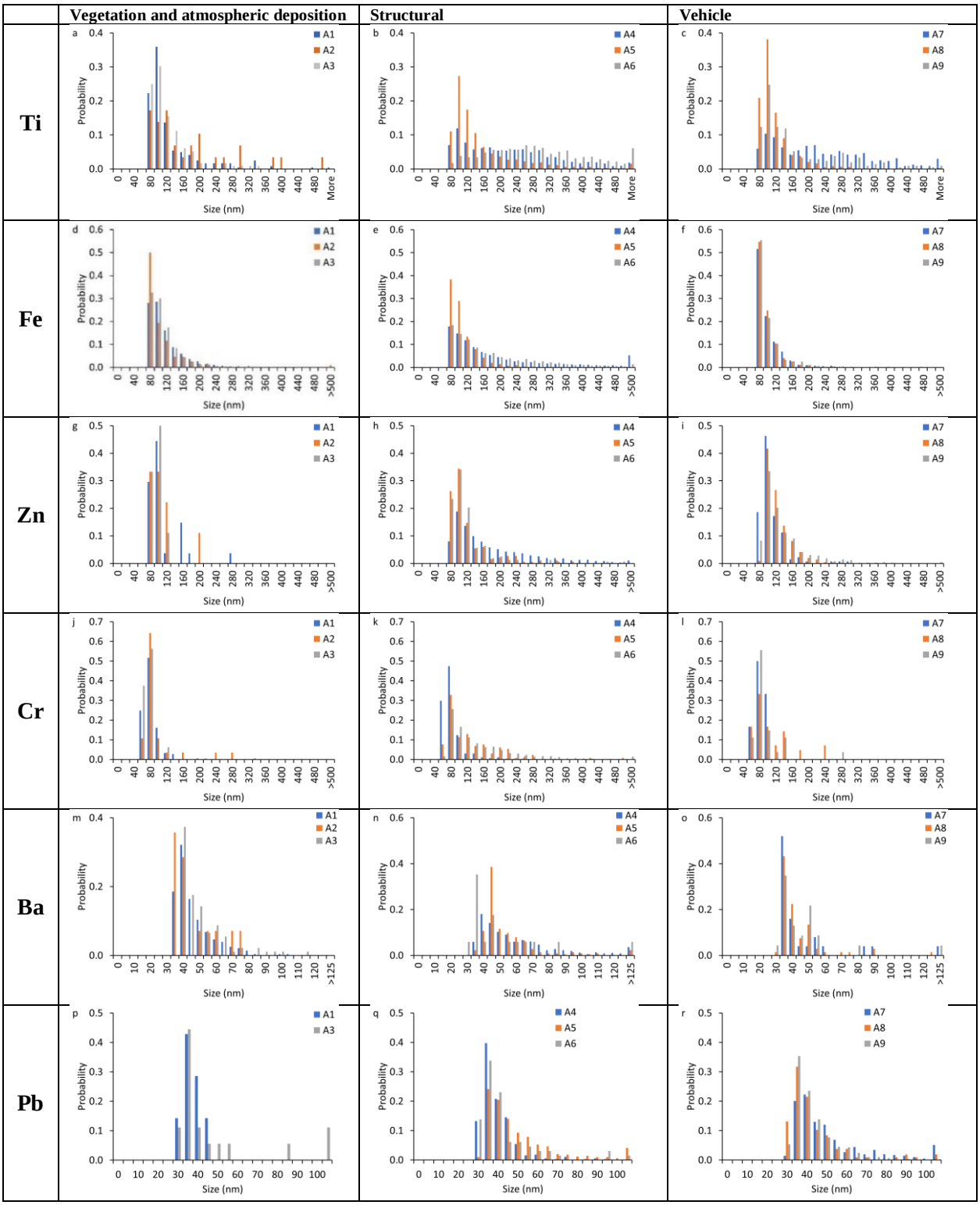

Figure S8. Particle size distribution of (a-c) Ti-bearing INMs, (d-f) Fe-bearing INMs, (g-i) Zn-bearing, and (j-l) Cr-bearing INMs, (m-o) Ba-bearing INMs, and (p-r) Pb-bearing INMs in (a, d, g, j, m, p) vegetation and atmospheric deposition ashes, (b, e, h, k, n, q) structural ashes, and (c, f, i, l, o, r) vehicle ashes.

1. Mahler RL. Nutrients plants require for growth. University of Idaho College of Agricultural and Life Science CIS. 2004;1124.
2. Reimann C, Koller F, Frengstad B, Kashulina G, Niskavaara H, Englmaier P. Comparison of the element composition in several plant species and their substrate from a 1 500 000-km2 area in Northern Europe. Science of the Total Environment. 2001;278(1-3):87-112.
3. Peralta-Videa JR, Lopez ML, Narayan M, Saupe G, Gardea-Torresdey J. The biochemistry of environmental heavy metal uptake by plants: Implications for the food chain. The International Journal of Biochemistry & Cell Biology. 2009;41(8):1665-77.
4. Brito DQ, Passos CJS, Muniz DH, Oliveira-Filho EC. Aquatic ecotoxicity of ashes from Brazilian savanna wildfires. Environmental Science and Pollution Research. 2017;24(24):19671-82.
5. GII Global Information. Titanium Dioxide (TiO2) - A Global Market Overview. https://www.giiresearch.com/report/inde1404118-titanium-dioxide-tio2-global-market-overview.html?utm_source=chatgpt.com. 2024. Report No.: CP040.
6. Linak E, Inoguchi Y. Chemical Economics Handbook: Titanium Dioxide‖. Menlo Park, CA, SRI Consulting. 2005.
7. Ober JA. Mineral resource of the month: Iron oxide pigments. Earth Magazine. 2008.
8. United States Geological Survey. Mineral commodity summaries 2021, 200 p., https://doi.org/10.3133/mcs2021.; 2021.
9. Chen AY-Y, Olsen T. Chromated copper arsenate–treated wood: a potential source of arsenic exposure and toxicity in dermatology. International Journal of Women's Dermatology. 2016;2(1):28-30.
10. de Medeiros Domingos D, Scussel R, Canever SB, Soares BQ, Angioletto E, Bernardin AM, et al. Toxicity of fly ash effluent from the combustion of (chromated copper arsenate)-treated wood. Cleaner Materials. 2022;3:100051.
11. Jambeck J, Weitz K, Solo-Gabriele H, Townsend T, Thorneloe S. CCA-Treated wood disposed in landfills and life-cycle trade-offs with waste-to-energy and MSW landfill disposal. Waste Management. 2007;27(8):S21-S8.
12. Helsen L, Van den Bulck E, Mullens S, Mullens J. Low-temperature pyrolysis of CCA-treated wood: thermogravimetric analysis. Journal of Analytical and Applied Pyrolysis. 1999;52(1):65-86.
13. Helsen L, Van den Bulck E. Review of disposal technologies for chromated copper arsenate (CCA) treated wood waste, with detailed analyses of thermochemical conversion processes. Environmental pollution. 2005;134(2):301-14.
14. Solo-Gabriele HM, Townsend TG, Messick B, Calitu V. Characteristics of chromated copper arsenate-treated wood ash. Journal of Hazardous Materials. 2002;89(2):213-32.
15. United States Environmental Protection Agency. Chromated Arsenicals (CCA), https://www.epa.gov/ingredients-used-pesticide-products/chromated-arsenicals-cca2024 03/03/2024.
16. Sharma CP. Engineering materials: properties and applications of metals and alloys: PHI Learning Pvt. Ltd.; 2003.
17. Habashi F. Alloys: preparation, properties, applications: John Wiley & Sons; 2008.
18. King M, Ramachandran V, Prengaman RD, DeVito SC, Breen J, Staff Ub. Lead and lead alloys. Kirk-Othmer Encyclopedia of Chemical Technology. 2000.
19. Bodí MB, Martin DA, Balfour VN, Santín C, Doerr SH, Pereira P, et al. Wildland fire ash: production, composition and eco-hydro-geomorphic effects. Earth-Science Reviews. 2014;130:103-27.
20. Alshehri T, Wang J, Singerling SA, Gigault J, Webster JP, Matiasek SJ, et al. Wildland-urban interface fire ashes as a major source of incidental nanomaterials. Journal of Hazardous Materials. 2023;443:130311.

21. Ormeno E, Cespedes B, Sanchez IA, Velasco-García A, Moreno JM, Fernandez C, et al. The relationship between terpenes and flammability of leaf litter. Forest Ecology and Management. 2009;257(2):471-82.
22. Saura-Mas S, Paula S, Pausas J, Lloret F. Fuel loading and flammability in the Mediterranean Basin woody species with different post-fire regenerative strategies. International Journal of Wildland Fire. 2010;19(6):783-94.
23. DeBano LF, Neary DG, Ffolliott PF. Fire effects on ecosystems: John Wiley & Sons; 1998.
24. Baalousha M, Desmau M, Singerling S, Webster JP, Matiasek S, Stern MA, et al. Discovery and potential ramifications of reduced iron-bearing nanomaterials—magnetite, wüstite, and zero valent iron—in wildland-urban interface fire ashes. Environmental Science Nano. 2022;9(4136):4149.
25. Bland GD, Lowry GV. Multistep method to extract moderately soluble copper oxide nanoparticles from soil for quantification and characterization. Analytical Chemistry. 2020;92(14):9620-8.
26. Baalousha M, Wang J, Erfani M, Goharian E. Elemental fingerprints in natural nanomaterials determined using SP-ICP-TOF-MS and clustering analysis. Science of The Total Environment. 2021;792:148426.
27. Rudnick R, Gao S, Holland H, Turekian K. Composition of the continental crust. The crust. 2003;3:1-64.
28. Wang J, Nabi MDM, Erfani M, Goharian E, Baalousha M. Identification and quantification of anthropogenic nanomaterials in urban rain and runoff using single particle-inductively coupled plasma-time of flight-mass spectrometry. Environmental Science Nano. 2022;9:714-29.